BOLETIN DE LA SOCIEDAD ESPAÑOLA DE
Cerámica y Vidrio
www.elsevier.es/bsecv

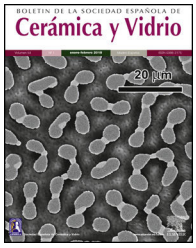

# Synthesis, structure, microstructure, and electrical properties of $Ce_{0.81}Nd_{0.095}Sm_{0.095}O_{2-\delta}$

*Somoju Ramesh*[a,*], *Mahadevappa Naganathappa*[a], *Jeevan Vemula*[b]

[a] *Department of Physics, GITAM School of Science, GITAM (Deemed to be University), Telangana 502329, India*
[b] *Department of Mechanical Engineering, GITAM School of Technology, GITAM (Deemed to be University), Telangana 502329, India*

ARTICLE INFO

*Article history:*
Received 12 August 2020
Accepted 2 March 2021
Available online 12 April 2021

*Keywords:*
Chemical synthesis
XRD
Ceramics
Electrolyte

ABSTRACT

Maltose and pectin-assisted low-temperature combustion modified sol–gel process was employed to synthesize nanopowders of $Ce_{0.8}Sm_{0.2}O_{2-\delta}$ (SDC 20), $Ce_{0.81}Nd_{0.095}Sm_{0.095}O_{2-\delta}$ (NSDC). The sample's powder was sintered at 1250 °C for 6 h to form dense ceramics with a relative density greater than 95%. The Rietveld refinement of powder XRD patterns indicates a single-phase material with a cubic fluorite structure. The Raman spectroscopy studies confirm solid solution with evidence of more oxygen vacancies in sample NSDC to sample SDC 20. The SEM images of the samples show a high-dense surface with few pores. The EDX results confirm the sample's chemical composition. Impedance measurements were carried out to study electrical properties. The NSDC sample showed improved conductivity ($3.06 \times 10^{-2}$ S/cm at 600 °C) over SDC 20 ($2.16 \times 10^{-2}$ S/cm at 600 °C) with lower activation energy (0.81 eV). Specific grain ($\sigma^*_g$) and grain boundary ($\sigma^*_{gb}$) conductivity values were calculated using porosity corrections to the Bricklayer model.



## Síntesis, estructura, microestructura y propiedades eléctricas de $Ce_{0,81}Nd_{0,095}Sm_{0,095}O_{2-\delta}$

*Palabras clave:*
Síntesis química
XRD
Cerámica
Electrólito

RESUMEN

Se empleó un proceso sol-gel modificado por combustión a baja temperatura asistido por maltosa y pectina para sintetizar nanopolvos de $Ce_{0,8}Sm_{0,2}O_{2-\delta}$ (SDC 20), $Ce_{0,81}Nd_{0,095}Sm_{0,095}O_{2-\delta}$ (NSDC). El polvo de la muestra se sinterizó a 1250 °C durante 6 h para formar cerámicas densas con una densidad relativa superior al 95%. El refinamiento de Rietveld de los patrones de XRD en polvo indica un material monofásico con una estructura de fluorita cúbica. Los estudios de espectroscopia Raman confirman la solución sólida con evidencia de más vacantes de oxígeno en la muestra NSDC a la muestra SDC 20. Las imágenes SEM de las muestras muestran una superficie de alta densidad con pocos poros. Los

* *Corresponding author.*
E-mail address: ramesh.ou1@gmail.com (S. Ramesh).
https://doi.org/10.1016/j.bsecv.2021.03.001

resultados de EDX confirman la composición química de la muestra. Se realizaron mediciones de impedancia para estudiar las propiedades eléctricas. La muestra de NSDC mostró una conductividad mejorada ($3{,}06 \times 10^{-2}$ S/cm a 600 °C) sobre SDC 20 ($2{,}16 \times 10^{-2}$ S/cm a 600 °C) con menor energía de activación (0,81 eV). Los valores específicos de conductividad de grano ($\sigma^*_g$) y del límite de grano ($\sigma^*_{gb}$) se calcularon utilizando correcciones de porosidad al modelo Bricklayer.



## Introduction

Solid electrolyte materials play a significant and vital role in solid oxide fuel cells (SOFCs). SOFCs convert chemical energy to electrical energy as long as the fuel is supplied [1,2]. SOFCs are known for clean, green, and efficient energy conversion. SOFC consists of an anode, cathode, and electrolyte materials as main parts [3]. An electrolyte material should have a higher density and electrical conductivity; for example, YSZ (yttrium stabilized zirconia) needs higher operating temperatures, i.e., more than 800 °C, to reach optimum conductivity. Materials selection is not that easy at such high operating temperatures where specific problems can occur like micro-cracks, materials degradation, chemical instability, and thermal instability across cell components [4–6].

In search of advanced alternate materials to bring down the operating temperature into the region 500–700 °C, doped cerium oxide ($CeO_2$) is a suitable candidate. $CeO_2$ is a poor ionic conductor ($10^{-5}$ S/cm at 600 °C) [3,5]. However, its conductivity could be improved by doping rare earth or alkaline earth materials. Besides, structural changes also play an important role in understanding ionic conductivity since it depends on oxygen vacancies [5]. Cerium oxide structure is cubic fluorite. When ceria is doped with dopants, solid solution formation without affecting its structure is essential to optimize the electrical properties.

The sample composition selection is based on the density functional theory (DFT) results reported by Anderson et al. [7]. Anderson et al. have suggested two combinations of dopants, i.e., Pr/Gd or Nd/Sm. When these dopants doped into ceria in the ratio 1:1, improved conductivity with lower activation energy values were reported theoretically. In the present study, Nd/Sm combination is selected in the ratio of 1:1. Furthermore, the average atomic number of Nd (61) and Sm (62) is 61.5, which is correlated to the critical ionic radius ($r_c$) [8,9]. Kim [10] reported that the dopants selection should be based on the critical radius ($r_c$) (for trivalent dopants, 1.04 Å) to optimize the ionic conductivity. However, it is not possible to explain the electrical properties only based on the critical radius ($r_c$) [9,11].

The sample preparation method plays a vital role in preparing dense ceramic electrolytes. For example, Omer et al. [12] have synthesized the samples $Sm_{x/2}Nd_{x/2}Ce_{1-x}O_{2-\delta}$ through the solid-state reaction method and obtained the dense ceramic samples by sintering at 1600 °C for 12 h. Such high temperatures result in micro-cracks on the surface, considerable grain growth, and sample composition instability. Liu et al. [13] reported citric acid–nitrate low-temperature combustion process for the system $Ce_{0.9}(Sm_xNd_{1-x})_{0.1}O_{1.95}$, and

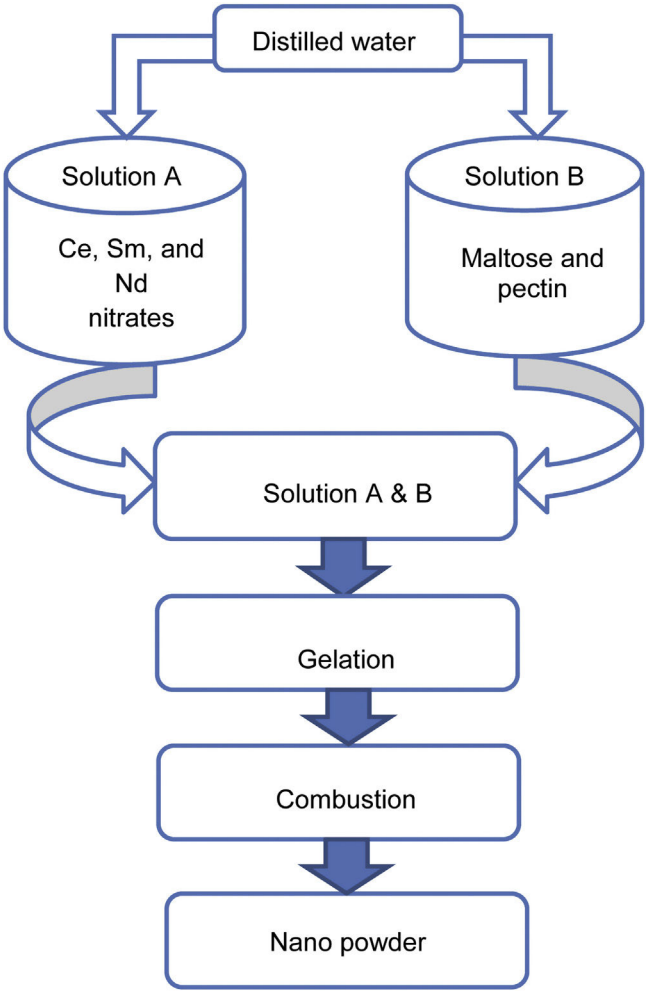


**Fig. 1 – Modified sol–gel process flow chart of SDC 20 and NSDC samples.**

samples were sintered at 1350 °C for 4 h. Coles-Aldridge and Baker [9] reported a citrate complexation process for the system $Ce_{0.8}Sm_xGd_yNd_zO_{1.9}$ and sintered samples at 1450 °C for 4 h. Arabaci et al. [14] synthesized $Nd_{0.20}Sm_xCe_{0.8-x}O_{1.9-x/2}$ samples by a polyol process and sintered at 1400 °C for 6 h. Li et al. [15] reported a citrate sol–gel method for $Ce_{0.8}Sm_{0.1}Nd_{0.1}O_{2-\delta}$ and sintered at 1500 °C for 4 h. A modified sol–gel process using maltose and pectin [16,17] has been employed to prepare the samples to overcome these problems in the present study. This method is very simple, environment

friendly, and more control over the particle size with uniform distribution.

In the present study, $Ce_{0.8}Sm_{0.2}O_{2-\delta}$ (SDC 20), $Ce_{0.81}Nd_{0.095}Sm_{0.095}O_{2-\delta}$ (NSDC) samples are prepared through a modified sol–gel process using maltose and pectin as chelating and gel agents [16,17]. The present investigation aims to prepare dense ceramics at sintering temperatures lower than reported [9,12–15] and study their structural, microstructural, and electrical properties.

## Experimental method

A modified sol–gel process using maltose and pectin was carried out to synthesize the samples SDC 20 and NSDC. Ce, Sm, and Nd nitrates were dissolved in distilled water under continuous stirring in a beaker. The synthesis procedure can be seen in Fig. 1, and details can be found elsewhere [16,17]. Maltose and pectin solution is slowly dripped into nitrates' solution by continuously stirring the solution up to 1 h to avoid particles' agglomeration and solidification into crystals. The adequately mixed solution was kept on a magnetic stirrer at 85 °C until forming a gel. The gel was then placed on a hot plate at 80 °C for 21 h, resulting in pale yellow colour powder.

Furthermore, the powder was calcined at 600 °C for 2 h, and the powder was properly ground to get a fine powder. The powder was then pressed uni-axially into circular pellets, and then sample pellets were sintered in air at 1250 °C for 6 h. The Archimedes method was used to measure density. The sintered sample's relative density was more than 95%.

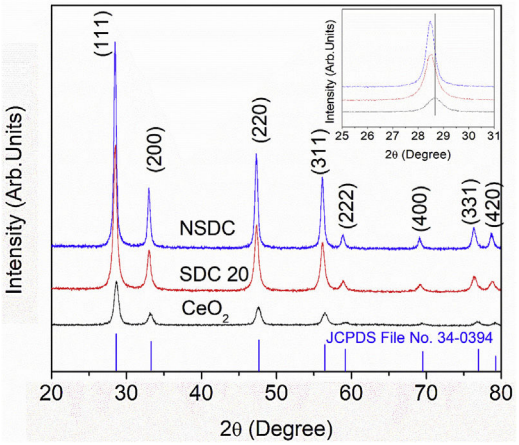


**Fig. 2 – The powder XRD patterns of SDC 20 and NSDC samples.**

The powder XRD patterns were recorded by the BRUKER D8 instrument. Topaz software was used for Rietveld refinement of powder XRD patterns. A Raman spectrometer (LABRAM-HR using a laser excitation line of 514.5 nm at room temperature) was used to record the Raman spectra. The sample's surface morphology was recorded using a scanning electron microscope (FE-SEM, ZEISS Sigma 500 VP). Sample composition analysis was observed by an energy-dispersive X-ray spectrometer (EDX attached with FE-SEM). An Agilent precision impedance analyzer (4294 A) was used to measure electrical properties. The measuring frequency range was between 42 Hz and 5 MHz on dense sintered pellets. The electrical con-

**Table 1 – Structural information of SDC 20 and NSDC samples.**

| Parameter | $CeO_2$ | SDC 20 | NSDC |
|---|---|---|---|
| *Structure* | Cubic | Cubic | Cubic |
| *Space group* | $Fm\bar{3}m$ | $Fm\bar{3}m$ | $Fm\bar{3}m$ |
| $R_p$ | 5.340 | 5.401 | 5.422 |
| $R_{wp}$ | 6.25 | 7.32 | 7.22 |
| $R_{exp}$ | 5.55 | 6.47 | 6.91 |
| GOF | 1.12 | 1.13 | 1.04 |
| *Lattice parameter, a* (Å) | 5.411 (0.002) | 5.421 (0.003)5.423 (Ref. [9]) | 5.439 (0.002)<br>5.440 (Ref. [15])<br>5.441 (Ref. [9]) |
| *Volume* ($a^3$) | 158.428 | 159.308 | 160.90 |
| *Average crystallite size* (nm) | 17 | 15 | 16 |
| *r.m.s strain* | $6 \times 10^{-4}$ | $5.24 \times 10^{-5}$ | $4.63 \times 10^{-5}$ |
| *Ce—O bond length* (Å) | 2.344 | 2.348 | 2.350 |
| **Atomic coordinate** | | | |
| *Ce (4a site)* | | | |
| (x y z) | (0 0 0) | (0 0 0) | (0 0 0) |
| Occupancy | 0.9983 | 0.8012 | 0.8104 |
| *Sm (4a site)* | | | |
| (x y z) | – | (0 0 0) | (0 0 0) |
| Occupancy | – | 0.1988 | 0.0948 |
| *Nd (4a site)* | | | |
| (x y z) | – | – | (0 0 0) |
| Occupancy | – | – | 0.0948 |
| *O (8c site)* | | | |
| (x y z) | (1/4 1/4 1/4) | (1/4 1/4 1/4) | (1/4 1/4 1/4) |
| Occupancy | 0.9901 | 0.9199 | 0.9251 |

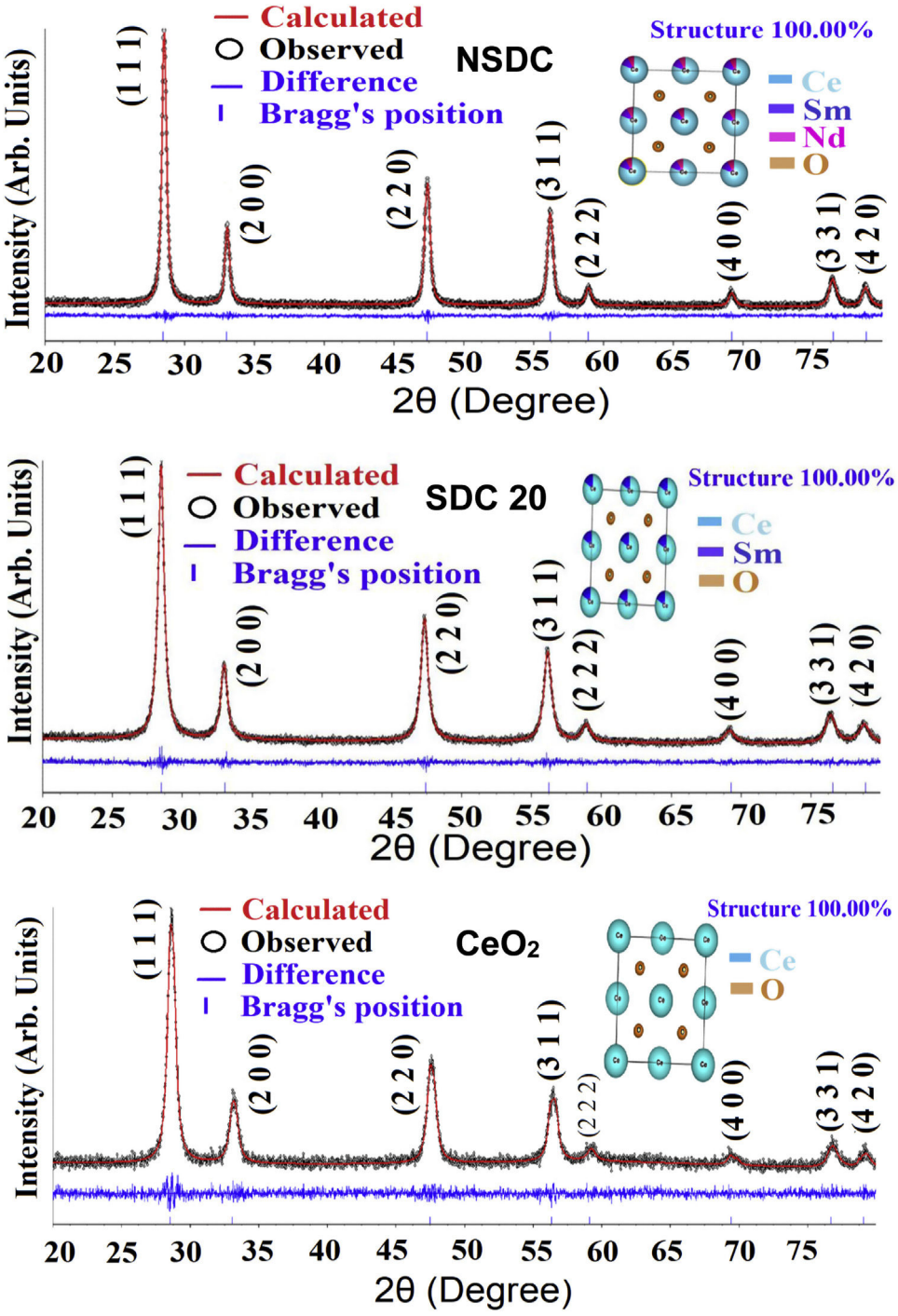


**Fig. 3 – The Rietveld refinement of powder XRD patterns SDC 20 and NSDC samples at 600 °C.**

ductivity measurements were taken at various temperatures between 250 and 700 °C in the air. Sample pellets surface was coated with silver paste and dried in the oven at 150 °C for 2 h.

## Results and discussion

### *Structural characterization*

Fig. 2 shows the powder XRD patterns of SDC 20 and NSDC samples. It shows a cubic fluorite structure with a space group $Fm\bar{3}m$ (JCPDS File No. 34-0394). The doping of $Nd^{3+}$ and $Sm^{3+}$ into $Ce^{4+}$ would result in a shift in the doped ceria peaks. This shift shows that the lattice parameter of the NSDC sample is increased over SDC 20. When larger ionic radii of dopants ($Sm^{3+}$,1.07 Å, and $Nd^{3+}$, 1.10 Å) doped into a host of smaller ionic radii ($Ce^{4+}$, 0.97 Å), it results in an expansion in the host lattice [9,12]. The lattice parameter of the NSDC sample is 5.439 Å (±0.002), and it is nearer to the reported values (Table 1) [9,15]. However, the reported composition ($Ce_{0.80}Nd_{0.1}Sm_{0.1}O_{2-\delta}$)

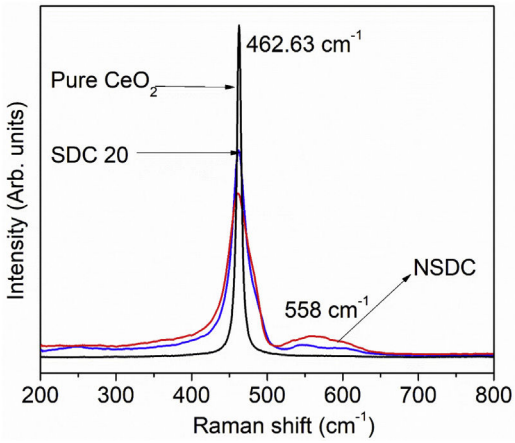


**Fig. 4 – The Raman spectra of SDC 20 and NSDC samples.**

of the samples is not the same as the present sample ($Ce_{0.81}Nd_{0.095}Sm_{0.095}O_{2-\delta}$).

The reflection from the (1 1 1) plane was used to calculate the average crystallite size. The average crystallite size ($D_{XRD}$) was calculated using Scherrer's equation:

$$D_{XRD} = \frac{0.9\lambda}{\beta \cos\theta},$$

where $\lambda$ is the wavelength of the radiation, $\theta$ is the diffraction angle, and $\beta$ is the full-width at the half maximum. $\beta$ broadening depends on instrumental broadening and sample size broadening. $\beta$ is corrected using the relation ($\beta^2_{sample} = \beta^2_{total} - \beta^2_{instrument}$).

The average crystallite size values of SDC 20 and NSDC samples are presented in Table 1. The Rietveld refinement of powder XRD patterns SDC 20 and NSDC samples is shown in Fig. 3. It is noticed that the difference between experimental data and calculated data is small (i.e., almost a line). The fitting profile parameters like space group, profile, structure, $R_p$, $R_w$, $R_{exp}$, and goodness of fit (GOF) are shown in Table 1. The dopants Nd and Sm were positioned at site 4a with coordinate (0 0 0) of Ce, and oxygen was positioned at site 8c with coordinate (1/4 1/4 1/4). The occupancy numbers are given in Table 1. VESTA images are included in Fig. 3 (insets).

### *Raman spectroscopy*

Fig. 4 presents the Raman spectra of SDC 20 and NSDC samples. It can be seen from Fig. 4 that for pure $CeO_2$, there is only one vibrational mode at 462.63 $cm^{-1}$, and it is related to $F_{2g}$ symmetry (cubic phase) [18]. Furthermore, it is observed that there is one more extra band present at around 558 $cm^{-1}$. This additional band indicates the formation of oxygen vacancies. i.e., when $Nd^{3+}$ and $Sm^{3+}$ doped into the ceria matrix, oxygen vacancies are introduced. Besides, a decrease in intensity for the samples SDC 20 and NSDC over pure ceria is noticed. There is a shift towards lower frequency due to the ionic radius difference between host ($Ce^{4+}$, 0.97 Å) and dopants ($Sm^{3+}$, 1.07 Å, and $Nd^{3+}$, 1.10 Å). Raman spectra results support XRD results as solid solution formation and give evidence for the more oxygen vacancies for the sample NSDC over SDC 20.

### *Morphological characterization*

Fig. 5(a) and (b) shows the SEM images at temperatures 600 °C and 1000 °C. The density of the sample is increasing with temperature. The SEM image (Fig. 5(c)) provides the information that small pores were present on the broken pellet surface. Fig. 5(d) shows the SEM photograph of NSDC of specimens at 1250 °C. The sample surface shows grains clearly and a highly dense surface. The mean line intercept method was used to calculate the average grain size, and its value is 1.54 μm. Besides, there are few grains in size range of 0.43–0.55 μm. Fig. 5(e) presents the EDX element composition of NSDC samples. It is noticed that Ce, Nd, and Sm are present in the final sample as per the weight calculation.

### *Electrical properties*

To understand the electrical properties response of electrolyte material, a.c. impedance spectroscopy is a powerful tool to study grain, grain boundary, and electrode contributions to the total ionic conductivity. It is possible to study the transport properties from impedance studies by analyzing the real (resistive) and imaginary (reactive) parts separately.

Fig. 6(a) and (b) shows the typical Nyquist plots of NSDC samples at different temperatures. It is noticed that there are two well-resolved semi-circles in Fig. 6(a). A high-frequency semi-circle contributes to grain resistance ($R_g$), and a medium frequency semi-circle contributes to grain boundary resistance ($R_{gb}$). The grain and grain boundary resistance sum is the total resistance ($R_t = R_g + R_{gb}$) [19]. As the temperature is increased, both grain and grain boundary resistances decreased. Grain resistance arc is seen partially and not resolved properly after 350 °C temperature in Fig. 6(b) due to frequency limit. The resistor–capacitor model was used to fit the impedance spectra (EIS software). CPE elements replace the capacitor due to different grain size distribution.

Fig. 6(c) presents the typical Nyquist plots for the samples SDC 20 and NSDC at 250 °C. Compared with the SDC 20 sample, grain resistance is higher for the NSDC sample and lower grain boundary resistance; this shows that Sm and Nd co-dopants could decrease the grain boundary resistance over SDC 20 sample. However, Coles-Aldridge and Baker [9] reported that grain size varies with sintering temperature. i.e., with increasing sintering temperature, increase in grain size, and decrease in the grain boundary area, consequently, an increase in grain resistance with grain size and a decrease in grain boundary resistance. The total ionic conductivity $\sigma = l/RA$ is calculated using total resistance, $R_t = R_g + R_{gb}$, where $R_g$ is the grain resistance, $R_{gb}$ is the grain boundary resistance, $l$ is the thickness, and $A$ is the cross-sectional area.

Fig. 7(a)–(c) shows the Arrhenius nature of conductivity vs. inverse temperature for grain, grain boundary, and total electrical conductivity of SDC 20 and NSDC samples. Fig. 7(a) shows the grain conductivity is higher for the sample SDC 20 over the NSDC sample, whereas grain boundary conductivity is higher for the NSDC sample over SDC 20 sample, as shown in Fig. 7(b). Fig. 7(c) shows that the total electrical conductivity of the NSDC sample is higher than that of the sample SDC 20. Total electrical conductivity values of SDC 20 and NSDC

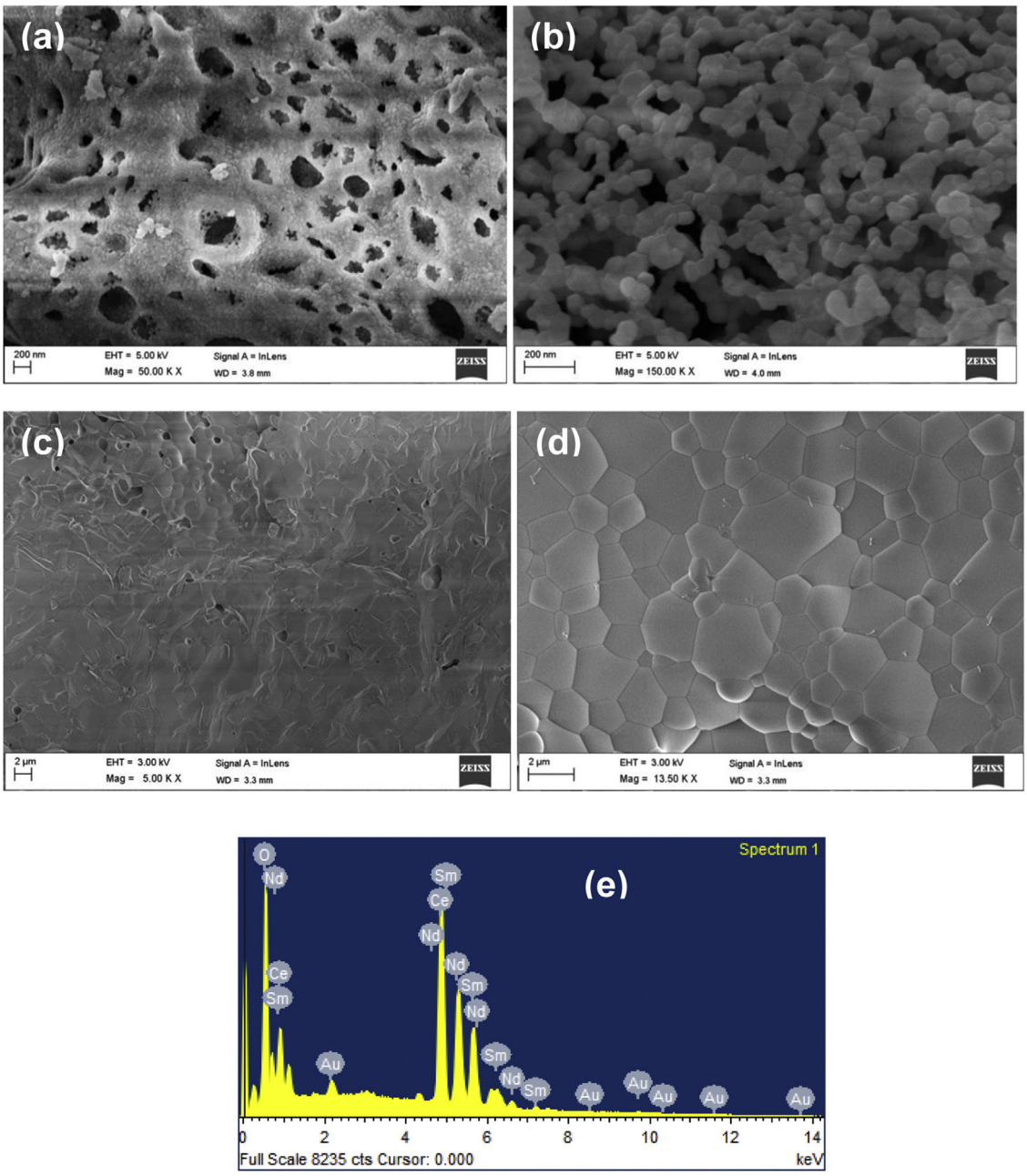


**Fig. 5 – SEM images of NSDC sample (a) 600 °C, (b) 1000 °C, (c) Broken pellet surface, (d) 1250 °C and (e) EDS element mapping.**

samples are presented in Table 2. When $Sm^{3+}$ and $Nd^{3+}$ doped into ceria, oxygen vacancies are created, which improves the ionic conductivity [3,5,6,9]. These equations are written in KrÖger-Vink notation [3,5], ($V_O^{\bullet\bullet}$) = oxygen vacancy concentration, $Nd'_{Ce}$ or $Sm'_{Ce}$ = $Nd^{3+}$ or $Sm^{3+}$ doped into host $Ce^{4+}$. The re-orientation process takes place due to $V_O^{\bullet\bullet}$, oxygen vacancy occupancy in the fluorite structure. $V_O^{\bullet\bullet}$, oxygen vacancy forms defect associate pairs with dopant cations ($Nd'_{Ce}$. $V_O^{\bullet\bullet}$, $Sm'_{Ce}$.$V_O^{\bullet\bullet}$) or ($Nd'_{Ce}$.$V_O^{\bullet\bullet}$.$Nd'_{Ce}$, $Sm'_{Ce}$.$V_O^{\bullet\bullet}$.$Sm'_{Ce}$) [20].

Fig. 7(a)–(c) presents grain, grain boundary, and total electrical conductivity curves and follows a straight-line character. Activation energy values were calculated by linear fitting the curves. The activation energy of the samples was calculated using Eq. (1):

$$\sigma = \frac{\sigma_o}{T}\exp\left(-\frac{E_a}{kT}\right) \quad (1)$$

where $E_a$ is the activation energy, $k$ is Boltzmann constant, and $\sigma_o$ is the pre-exponential factor.

From Fig. 7(c), it is noticed that there is a slope change above 500 °C ($T_c$, transition temperature). In the temperature ranges 250–500 °C, total activation energy is due to association and migration energy, whereas at higher temperatures, i.e., 550–700 °C, total activation energy is due to migration energy

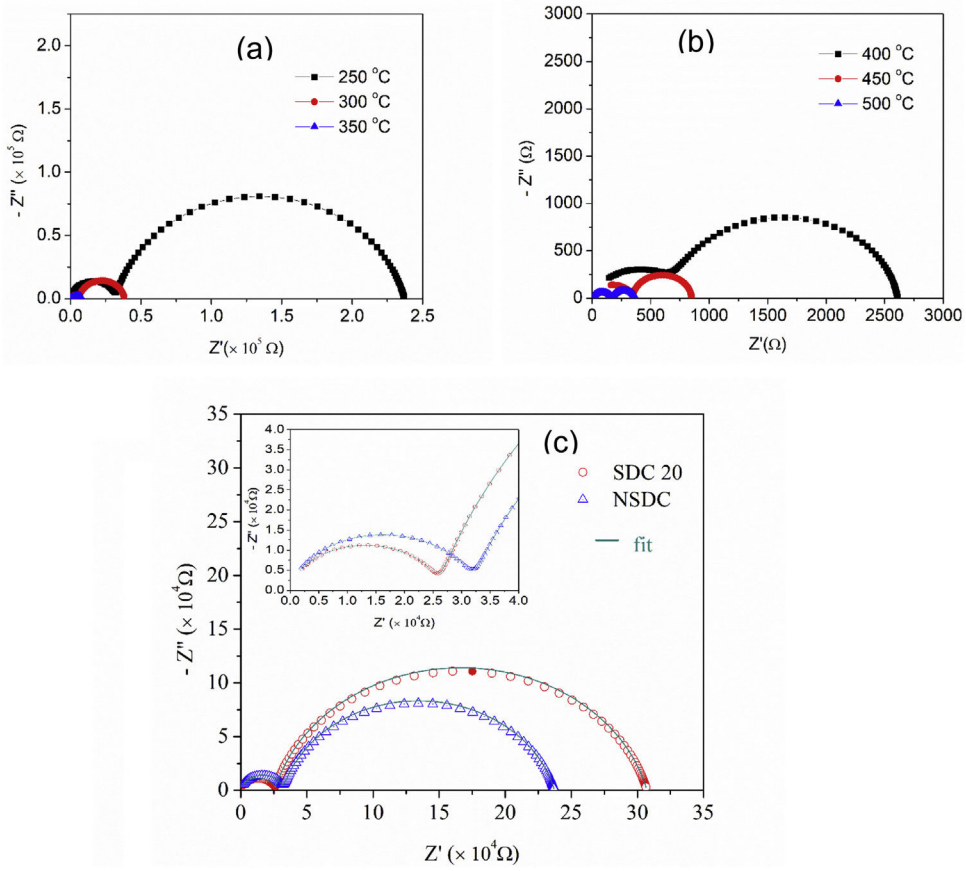


**Fig. 6 – (a and b) Nyquist plots of NSDC sample at different temperatures and (c) typical Nyquist plots of SDC 20 and NSDC samples at 250 °C.**

**Table 2 – Total electrical conductivity and activation energy values of SDC 20 and NSDC samples.**

| Temperature (°C) | SDC 20 | NSDC |
|---|---|---|
| | Total electrical conductivity, $\sigma_t$ (S/cm) | |
| 300 | $7.3090 \times 10^{-6}$ | $9.5991 \times 10^{-6}$ |
| 400 | $1.2254 \times 10^{-4}$ | $1.4086 \times 10^{-4}$ |
| 500 | $9.9364 \times 10^{-4}$ | $2.0248 \times 10^{-3}$ |
| 600 | 0.0061 | 0.0105 |
| 700 | 0.0216 | 0.0306 |
| | Activation energy (e V) Total conductivity | |
| (250–500) | 1.01 | 0.95 |
| (550–700) | 0.89 | 0.81 |

| | SDC 20 | | NSDC | |
|---|---|---|---|---|
| | Grain | Grain boundary | Grain | Grain boundary |
| (250–500) | 0.79 | 1.06 | 0.77 | 1.01 |

because most of the oxygen vacancies would dissociate [9,12]. The activation energies for grain, grain boundary, and total electrical conductivities are presented in Table 2. NSDC sample activation energy values are lower in comparison with the SDC 20 sample.

Table 3 presents the total electrical conductivity of SDC 20 and NSDC samples comparison with reported values. The total electrical conductivity values are matched with reported observations [21–31]. It is noticed from Table 3, slightly lower total electrical conductivity values than reported due to lower grain boundary conductivity contribution to the total electrical conductivity. However, grain boundary resistance could be decreased further by increasing the samples' density (grain boundary area decreased with increasing grain size at a higher density) [9]. In the present study, we could synthesize the nanopowders successfully through maltose–pectin

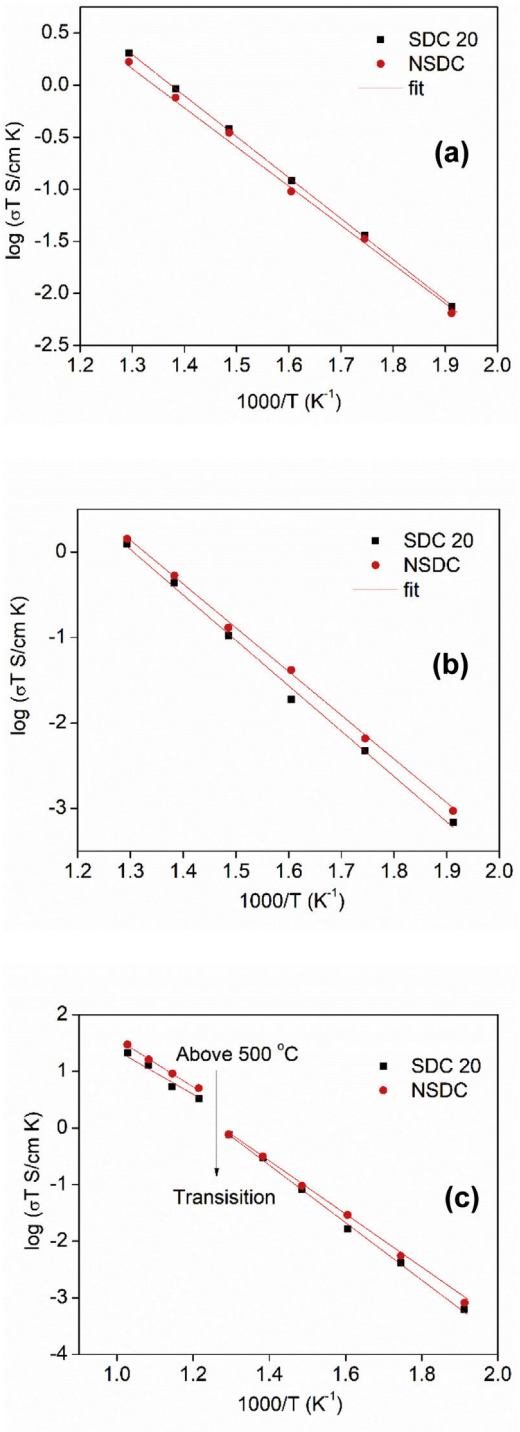


**Fig. 7 – Arrhenius nature of conductivity vs. 1000/*T* for SDC 20 and NSDC samples, (a) grain conductivity, (b) grain boundary, and (c) total conductivity.**

assisted modified sol–gel process. Dense ceramics are prepared by sintering the samples at 1250 °C for 6 h., The present sample's sintering temperature (density 95%) is lowered to 1250 °C (compared to 1350 °C), comparing with reported results [12–15]. However, as per the reports [9,13,15], grain boundary resistance could be decreased by increasing the sintering temperature. Electrical properties depend on the sample's synthesis method, structure, optimized sintering temperature, density, grain size, grain boundary area (grain boundary resistance contribution to total conductivity).

Pérez-Coll et al. [32] suggested the Bricklayer model with porosity corrections would be useful to study the electrical properties of lower density solid electrolyte materials. Fig. 8 shows the specific grain, specific grain boundary, normalized grain, and normalized grain boundary conductivity of SDC 20 and NSDC samples vs. 1000/*T*. Specific grain ($\sigma^*_g$), specific grain

**Table 3 – Electrical conductivity values comparison of SDC and NSDC samples.**

| Composition | Total conductivity, $\sigma_t$ (S/cm) | Activation energy (eV) | Reference |
|---|---|---|---|
| $Ce_{0.8}Sm_{0.2}O_{2-\delta}$ | $2.16 \times 10^{-2}$ (700 °C) | 0.89 | Present |
| $Ce_{0.81}Nd_{0.095}Sm_{0.095}O_{2-\delta}$ | $3.06 \times 10^{-2}$ (700 °C) | 0.81 | Present |
| $Ce_{0.80}Nd_{0.1}Sm_{0.1}O_{1.9}$ | $3.73 \times 10^{-2}$ (700 °C)(absolute value) | 0.90 | Coles-Aldridge [9] |
| $Ce_{0.80}Nd_{0.1}Sm_{0.1}O_{1.9}$ | $3.29 \times 10^{-2}$ (700 °C) | 1.02 | Kahlaoui [21] |
| $Ce_{0.80}Nd_{0.1}Y_{0.1}O_{1.9}$ | $3.17 \times 10^{-2}$ (700 °C) | 0.64 | Sha [22] |
| $Ce_{0.80}Nd_{0.08}Sm_{0.12}O_{1.9}$ | $3.90 \times 10^{-2}$ (700 °C) | 0.63 | Arabaci [23] |
| $Ce_{0.80}Nd_{0.1}Sm_{0.1}O_{2-\delta}$ | $1.32 \times 10^{-3}$ (600 °C) | 0.95 | Li [15] |
| SDC ($Ce_{0.8}Sm_{0.2}O_{2-\delta}$) | $2.0 \times 10^{-4}$ (600 °C) | 1.02 | Li [15] |
| NDC ($Ce_{0.8}Nd_{0.2}O_{2-\delta}$) | $2.8 \times 10^{-4}$ (600 °C) | 0.95 | Li [15] |
| SDC($Ce_{0.8}Sm_{0.2}O_{2-\delta}$) | $1.14 \times 10^{-2}$ (600 °C) | 0.65 | Liu [24] |
| $Ce_{0.8}Sm_{0.2}O_{2-\delta}$ | $2.22 \times 10^{-3}$ (600 °C) | 1.02 | Xiaomin[25] |
| $Ce_{0.8}Sm_{0.2}O_{2-\delta}$ | $1.79 \times 10^{-2}$ (600 °C) | 0.77 | Arabaci [26] |
| $Ce_{0.8}Gd_{0.2}O_{2-\delta}$ | $3.40 \times 10^{-2}$ (750 °C) | 0.62 | Arabaci [26] |
| $Ce_{0.8}Sm_{0.2}O_{2-\delta}$ | $2.36 \times 10^{-2}$ (700 °C) | 0.58 | Anwar [27] |
| $Ce_{0.9}Gd_{0.1}O_{2-\delta}$ | $1.13 \times 10^{-2}$ (700 °C) | 1.02 | Meisetti [28] |
| $Ce_{0.82}La_{0.06}Sm_{0.06}Gd_{0.06}O_{2-\delta}$ | $3.81 \times 10^{-2}$ (600 °C) | 0.55 | Venkataramana [29] |
| 8YSZ | $2.74 \times 10^{-4}$ (700 °C) | 0.74 | Rahmawati [30] |
| $Ce_{0.80}Nd_{0.1}Sm_{0.1}O_{1.9}$ | $3.15 \times 10^{-2}$ (600 °C) | 0.63 | Liu [31] |

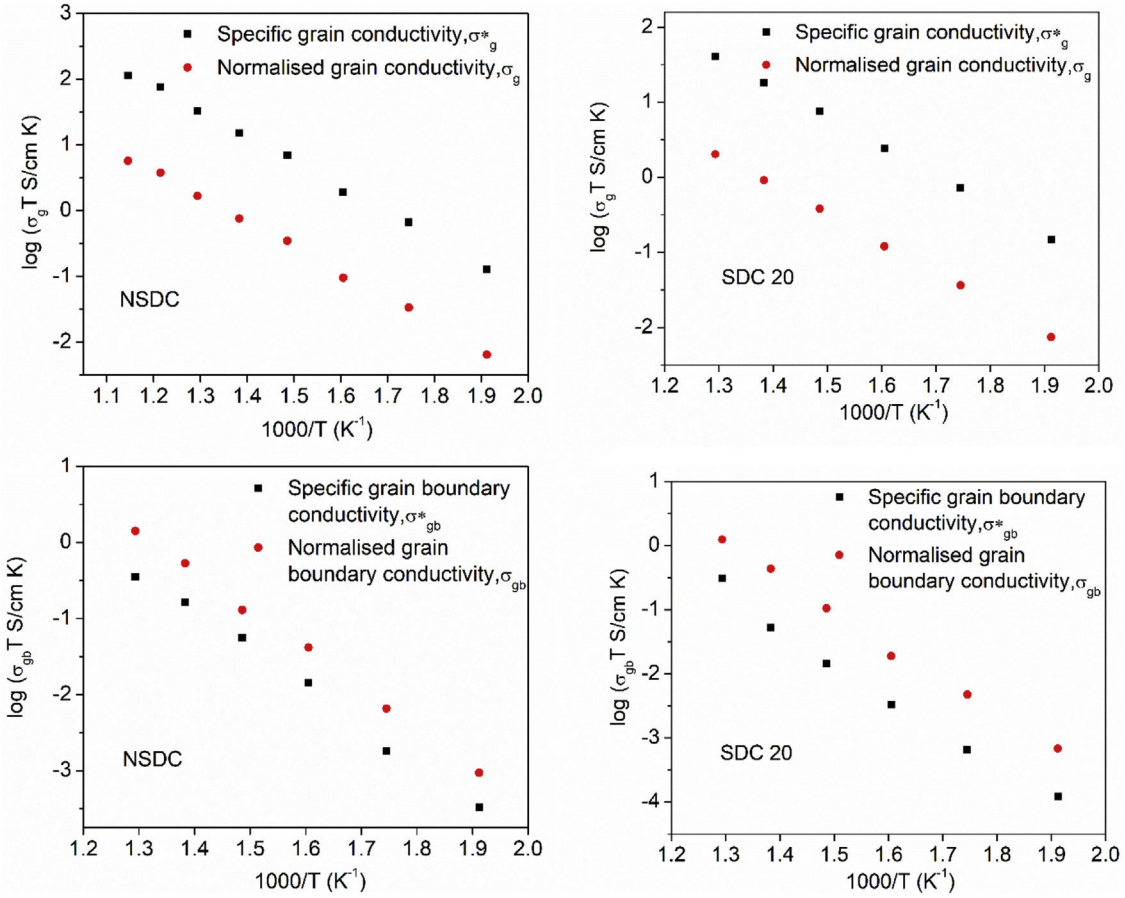


**Fig. 8 – Specific grain conductivity ($\sigma^* = L/(A.R_g.f_{por})$), specific grain boundary conductivity ($\sigma^* = L.d_{gb}/(A.R_{gb}.f_{por}.D)$), normalized grain conductivity ($\sigma_g = L/(A.R_g)$), and normalized grain boundary conductivity ($\sigma_{gb} = L/(A.R_{gb})$) of SDC 20 and NSDC samples vs. 1000/T.**

boundary ($\sigma^*_{gb}$) conductivity values were calculated using Eqs. (2) and (3) [32]:

$$\text{Specific grain conductivity, } \sigma^* g = \frac{L}{A.Rg.f_{por}} \quad (2)$$

$$\text{Specific grain boundary conductivity } \sigma^* = \frac{L.d_{gb}}{A.R_{gb}.f_{por}.D} \quad (3)$$

where $L$ is the thickness, $A$ is the cross-sectional area, $D$ is the average grain size, $d_g$ is the grain boundary thickness, $f_{por}$ is

the porosity factor, $R_g$ is the grain resistance, and $R_{gb}$ is the grain boundary resistance.

It is noticed from Fig. 8 that there is a porosity effect on grain and grain boundary conductivity; specific grain conductivity is higher than that of the normalized grain conductivity for the samples SDC 20 and NSDC, whereas specific grain boundary conductivity is lower than that the normalized grain boundary conductivity. Pérez-Coll et al. [32] pointed out that grain resistance depends on porosity, whereas grain boundary resistance depends on porosity and grain size. Porosity factor ($f_{por}$) is calculated using Eq. (4):

$$f_{por} = 1 - \left(\frac{\text{Experimental density}}{\text{Theoretical density}}\right) \quad (4)$$

Porosity results in the geometrical effects on sample resistance (grain and grain boundary resistance). However, it is noteworthy to say that the porosity correction is more useful for the samples whose relative density is lower, i.e., around 75–90%. The Bricklayer model is useful to explain the electrical properties of high dense ceramic electrolyte materials, whereas, for lower dense ceramic samples, it is not that useful [32] due to geometrical effect (like porosity, grain size). Using Eqs. (2)–(4), Pérez-Coll et al. [32] modified the Bricklayer model, and these modifications resulted in a specific grain and grain boundary conductivity (no geometrical effect on samples). It can be seen that from Fig. 8, specific grain conductivity contribution is higher than that of the specific grain boundary conductivity since grain boundary conductivity depends on density, grain size, and the porosity of the sample. Hence, therefore geometrical corrections would result in the real conductivity values of the samples.

## Conclusions

Samarium doped ceria, $Ce_{0.8}Sm_{0.2}O_{2-\delta}$ (SDC 20), Neodymium, and Samarium co-doped ceria $Ce_{0.81}Nd_{0.095}Sm_{0.095}O_{2-\delta}$ (NSDC) samples were synthesized successfully by the modified sol–gel method using maltose and pectin as chelating and gel agents. Rietveld refinement of XRD powder patterns confirms the cubic structure with a single phase. Oxygen vacancies and the formation of a solid solution were confirmed by Raman spectroscopy. High-dense ceramic samples were prepared by sintering at 1250 °C for 6 h with a high relative density (greater than 95%). SEM images were shown a high-dense surface with grains and consistent with the relative density. EDX confirms that Ce, Sm, Nd, and O are present in the final sample composition. The $Ce_{0.81}Nd_{0.095}Sm_{0.095}O_{2-\delta}$ (NSDC) sample shows higher total electrical conductivity, $3.06 \times 10^{-2}$ S/cm (600 °C), and lower activation energy (0.81 eV) than the SDC 20 sample, $2.16 \times 10^{-2}$ S/cm (600 °C) (0.89 eV). Specific grain and grain boundary conductivity results show porosity effect on normalized grain and grain boundary conductivity. Hence, the present sample is useful as an electrolyte for solid oxide fuel cell applications.

## Conflict of interest

The authors declare that they have no known competing financial interests or personal relationships that could have appeared to influence the work reported in this paper.

## REFERENCES


[1] N.Q. Minh, T. Takahashi, Science and Technology of Ceramic Fuel Cells, Elsevier Publications, Netherlands, 1995.

[2] R. Martínez-Bautistaa, S.M. Fernández-Valverdeb, A. Tejeda-Cruza, J.A. Chávez-Carvayara, Structural, morphological and electrical characterization of ceria-based nanostructured thin films obtained by ultrasonic spray pyrolysis, Boletín de la Sociedad Española de Cerámica y Vidrio 58 (2019) 38–47, http://dx.doi.org/10.1016/j.bsecv.2018.06.004.

[3] B.C.H. Steele, Appraisal of $Ce_{1-y}Gd_yO_{2-y/2}$ electrolytes for IT-SOFC operation at 500 °C, Solid State Ionics 129 (2000) 95, http://dx.doi.org/10.1016/S0167-2738(99)00319-7.

[4] J. Larmine, A. Dicks, Fuel Cell Systems Explained, John Wiley & Sons, London, 2000, pp. 166.

[5] H. Inaba, H. Tagawa, Ceria based solid electrolytes, Solid State Ionics 83 (1996) 1, http://dx.doi.org/10.1016/0167-2738(95)00229-4.

[6] J.A. Kilner, Fast oxygen transport in acceptor doped oxides, Solid State Ionics 129 (2000) 13, http://dx.doi.org/10.1016/S0167-2738(99)00313-6.

[7] D.A. Anderson, S.I. Simak, N.V. Skorodumova, I.A. Abrikosov, B. Johansson, Optimization of ionic conductivity in doped ceria, Proc. Natl. Acad. Sci. U. S. A. 103 (2006) 3518–3521, http://dx.doi.org/10.1073/pnas.0509537103.

[8] S. Omar, E. Wachsman, J. Nino, A co-doping approach towards enhanced ionic conductivity in fluorite-based electrolytes, Solid State Ionics 177 (2006) 3199–3203.

[9] A.V. Coles-Aldridge, R.T. Baker, Ionic conductivity in multiply substituted ceria-based electrolytes, Solid State Ionics 316 (2018) 9–19, http://dx.doi.org/10.1016/j.ssi.2017.12.013.

[10] D.J. Kim, Lattice parameters, ionic conductivities, and solubility limits in fluorite-structure MO2 oxide [M = $Hf^{4+}$, $Zr^{4+}$, $Ce^{4+}$, $Th^{4+}$, $U^{4+}$] solid solutions, J. Am. Ceram. Soc. 72 (1989) 1415, http://dx.doi.org/10.1111/j.1151-2916.1989.tb07663.x.

[11] S. Omar, E.D. Wachsman, J.L. Jones, J.C. Nino, Crystal structure–ionic conductivity relationships in doped ceria systems, J. Am. Ceram. Soc. 92 (2009) 2674–2681.

[12] S. Omer, E.D. Wachsman, J.C. Nino, Higher conductivity $Sm^{3+}$ and $Nd^{3+}$ co-doped ceria-based electrolyte materials, Solid State Ionics 178 (2008) 1890, http://dx.doi.org/10.1016/j.ssi.2007.12.069.

[13] B. Li, Y. Liu, X. Wei, W. Pan, Electrical properties of ceria Co-doped with $Sm^{3+}$ and $Nd^{3+}$, J. Power Sources 195 (2010) 969–976, http://dx.doi.org/10.1016/j.jpowsour.2009.09.001.

[14] A. Arabacı, M. Derb, M.F. Öksüzömerb, T.G. Altınçekiç, Characterization of Nd and Sm Co-doped $CeO_2$-based systems, Acta Phys. Pol. A 1 (2017) 78–81, http://dx.doi.org/10.12693/APhysPolA.131.78.

[15] S.P. Li, J.Q. Lu, P. Fang, M.F. Luo, Effect of oxygen vacancies on electrical properties of $Ce_{0.8}Sm_{0.1}Nd_{0.1}O_{2-\delta}$ electrolyte: an in situ Raman spectroscopic study, J. Power Sources 193 (2009) 93–98, http://dx.doi.org/10.1016/j.jpowsour.2008.12.022.

[16] C. Suciu, L. Gageab, A.C. Hoffmann, M. Mocean, Sol–gel production of zirconia nanoparticles with a new organic precursor, Chem. Eng. Sci. 61 (2006) 783, http://dx.doi.org/10.1016/j.ces.2006.09.006.
[17] Z. Wang, G.M. Kale, M. Ghadiri, Maltose and pectin assisted sol–gel production of $Ce_{0.8}Gd_{0.2}O_{1.9}$ solid electrolyte nanopowders for solid oxide fuel cells, J. Mater. Chem. 21 (2011) 16494, http://dx.doi.org/10.1039/C1JM12344K.
[18] J.R. McBride, K.C. Hass, B.D. Poindexter, W.H. Weber, Raman and X-ray studies of $Ce_{1-x}RE_xO_{2-y}$, where RE = La, Pr, Nd, Eu, Gd, and Tb, J. Appl. Phys. 764 (1994) 2435, http://dx.doi.org/10.1063/1.357593.
[19] J.E. Bauerle, Study of solid electrolyte polarization by a complex admittance method, J. Phys. Chem. Solids 30 (1969) 2657–2670, http://dx.doi.org/10.1016/0022-3697(69)90039-0.
[20] Sk. Anirban, T. Paul, P.T. Das, T.K. Nath, A. Dutta, Microstructure and electrical relaxation studies of chemically derived Gd–Nd co-doped nanocrystalline ceria electrolytes, Solid State Ionics 270 (2015) 73–83, http://dx.doi.org/10.1016/j.ssi.2014.12.011.
[21] M. Kahlaoui, S. Chefi, A. Inoubli, A. Madani, C. Chefi, Synthesis and electrical properties of co-doping with $La^{3+}$, $Nd^{3+}$, $Y^{3+}$, and $Eu^{3+}$ citric acid–nitrate prepared samarium-doped ceria ceramics, Ceram. Int. 39 (2013) 3873–3879.
[22] X. Sha, Z. Lü, X. Huang, J. Miao, L. Jia, X. Xin, W. Sue, Preparation and properties of rare earth co-doped $Ce_{0.8}Sm_{0.2-x}Y_xO_{1.9}$ electrolyte materials for SOFC, J. Alloys Compd. 424 (2006) 315–321.
[23] A. Arabaci, Effect of Er, Gd, and Nd co-dopants on the properties of Sm-doped ceria electrolyte for IT-SOFC, Metall. Mater. Trans. A (2017), http://dx.doi.org/10.1007/s11661-017-3990-4.
[24] Y. Liu, L. Fan, Y. Cai, W. Zhang, B. Wang, B. Zhu, Superionic conductivity of $Sm^{3+}$, $Pr^{3+}$, and $Nd^{3+}$ triple-doped ceria through bulk and surface two-step doping approach, ACS Appl. Mater. Interfaces 9 (2017) 23614–23623, http://dx.doi.org/10.1021/acsami.7b02224.
[25] L.I.N. Xiaomin, L. Qiuyue, Z.H.U. Lili, L.I.U. Xiaomei, Synthesis and characterization of $Ce_{0.8}Sm_{0.2-x}Pr_xO_{2-\delta}$ (x = 0.02–0.08) solid electrolyte materials, J. Rare Earths 33 (2015) 411–416, http://dx.doi.org/10.1016/S1002-0721(14)60434-8.
[26] A. Arabacı, T.G. Altınçekiç, M. Der, M.A.F. Öksüzömer, Preparation and properties of ceramic electrolytes in the Nd and Gd co-doped ceria systems prepared by Polyol method, J. Alloys Compd. 792 (2019) 1141–1149, http://dx.doi.org/10.1016/j.jallcom.2019.04.098.
[27] M. Anwar, S.A. Muhammed Ali, N.A. Baharuddin, N.F. Raduwan, A. Muchtar, Structural, optical and electrical properties of $Ce_{0.8}Sm_{0.2-x}Er_xO_{2-\delta}$ (x = 0–0.2) co-doped ceria electrolytes, Ceram. Int. 44 (2018) 13639–13648, http://dx.doi.org/10.1016/j.ceramint.2018.04.200.
[28] S. Medisetti, J. Ahn, S. Patil, A. Goel, Y. Bangaru, G.V. Sabhahit, G.U.B. Babu, J.H. Lee, H.P. Dasari, Synthesis of GDC electrolyte material for IT-SOFCs using glucose & fructose and its characterization, Nano-Struct. Nano-Objects 11 (2017) 7–12, http://dx.doi.org/10.1016/j.nanoso.2017.05.009.
[29] K. Venkataramana, C. Madhuri, Ch. Madhusudan, Y. Suresh Reddy, C. Vishnuvardhan Reddy, Investigation on micro-structural, structural, electrical and thermal properties of $La^{3+}$, $Sm^{3+}$ & $Gd^{3+}$ triple-doped ceria as solid electrolyte for intermediate temperature solid oxide fuel cell applications, J. Appl. Phys. 126 (2019) 144901–144911, http://dx.doi.org/10.1063/1.5113890.
[30] F. Rahmawati, I. Permadani, D.G. Syarif, S. Soepriyanto, Electrical properties of various composition of yttrium doped-zirconia prepared from local zircon sand, Int. J. Technol. 8 (2017) 939–946, http://dx.doi.org/10.14716/ijtech.v8i5.876.
[31] Y. Liu, W.B. Li, X. Wei, W. Pan, Citric–nitrate combustion synthesis and electrical conductivity of the $Sm^{3+}$ and $Nd^{3+}$ co-doped ceria electrolyte, J. Am. Ceram. Soc. 91 (2008) 3926–3930, http://dx.doi.org/10.1111/j.1551-2916.2008.02748.x.
[32] D. Pérez-Coll, E. Sánchez-López, G.C. Mather, Influence of porosity on the bulk and grain-boundary electrical properties of Gd-doped ceria, Solid State Ionics 181 (2010) 1033–1042, http://dx.doi.org/10.1016/j.ssi.2010.06.006.